



Iron isotope fractionation during mid-ocean ridge basalt (MORB) evolution: Evidence from lavas on the East Pacific Rise at 10°30'N and its implications

Shuo Chen^{a,b,c,*}, Yaoling Niu^{b,d,e,*}, Pengyuan Guo^{a,b,c}, Hongmei Gong^{a,b,c},
Pu Sun^{a,b,c}, Qiqi Xue^a, Meng Duan^{a,b,c}, Xiaohong Wang^{a,b,c}

^a Institute of Oceanology, Chinese Academy of Sciences, Qingdao 266071, China

^b Laboratory for Marine Geology, Qingdao National Laboratory for Marine Science and Technology, Qingdao 266061, China

^c Center for Ocean Mega-Science, Chinese Academy of Sciences, 7 Nanhai Road, Qingdao 266071, China

^d Department of Earth Sciences, Durham University, Durham DH1 3LE, UK

^e China University of Geosciences, Beijing 100083, China

Received 23 June 2019; accepted in revised form 17 September 2019; Available online 25 September 2019

Abstract

Whether the Earth's mantle has a chondritic $\delta^{56}\text{Fe}$ (deviation in $^{56}\text{Fe}/^{54}\text{Fe}$ from the IRMM-014 standard in parts per thousand) value or not remains under debate. The current view is that the observed average $\delta^{56}\text{Fe}$ of mid-ocean ridge basalts (MORB) cannot be explained by partial melting of mantle source with chondritic value alone. Here, we report Fe isotope compositions on 29 MORB glasses sampled along a flowline traverse across the East Pacific Rise (EPR) axis at 10°30'N. These glasses show large MgO variation (1.8–7.4 wt.%) that forms a compositional continuum resulting from varying extent of fractional crystallization, which is accompanied by systematic Fe isotopic variation. Fractional crystallization modeling suggests that early crystallization of olivine, pyroxene and plagioclase gives rise to an iron enrichment trend and an increase in $\delta^{56}\text{Fe}$. Once Fe-Ti oxides appear on the liquidus and begin to crystallize, the FeO^t and TiO₂ contents of the residual melt decrease rapidly, which lead to a slight decrease in $\delta^{56}\text{Fe}$. These observations indicate that significant Fe isotope fractionation can indeed take place during MORB melt evolution. Hence, $\delta^{56}\text{Fe}$ values of variably evolved MORB melts do not represent those of primary MORB melts and thus cannot be used to infer mantle source Fe isotope compositions. Importantly, $\delta^{56}\text{Fe}$ values of primary MORB melts after correction for the effect of fractional crystallization can be well reproduced by mantle melting. Therefore, our study supports the idea that the Fe isotope composition of the accessible Earth is close to be chondritic. We note that conclusion would assume that the core, which takes up ~90% of the Earth's Fe, must have a chondritic Fe isotope composition.

© 2019 Elsevier Ltd. All rights reserved.

Keywords: Fe isotope; Mid-ocean ridge basalts; East Pacific Rise; Bulk silicate earth

1. INTRODUCTION

The Fe isotope composition of the bulk silicate Earth (BSE) has been the subject of debate for ~20 years (see Dauphas et al., 2017). For instance, the average $\delta^{56}\text{Fe}$ value of mid-ocean ridge basalts (MORB), oceanic island basalts (OIB) and continental basalts are ~0.1‰ higher relative to

* Corresponding authors.

E-mail addresses: shuochen@qdio.ac.cn (S. Chen), yaoling.niu@durham.ac.uk (Y. Niu).

chondrites (Poitrasson et al., 2004; Weyer and Ionov, 2007; Teng et al., 2013). This was initially interpreted as resulting from Fe isotope fractionation during iron vaporization associated with the giant Moon-forming impact event (Poitrasson et al., 2004) or high-temperature and high-pressure equilibrium fractionation between metal and silicate during core formation (Polyakov, 2009; Williams et al., 2012). These models, however, remain debated (Poitrasson et al., 2009; Hin et al., 2012; Shahar et al., 2015; Elardo et al., 2019). In contrast, subsequent studies of peridotite xenoliths from different settings (Williams et al., 2004, 2005; Weyer et al., 2005; Weyer and Ionov, 2007; Dauphas et al., 2009a; Zhao et al., 2010; Huang et al., 2011; Zhao et al., 2012; Poitrasson et al., 2013) and komatiites or picrites produced by large degree of mantle melting (Dauphas et al., 2010; Hibbert et al., 2012; Nebel et al., 2014; McCoy-West et al., 2018) showed that, despite large variation, these rocks have $\delta^{56}\text{Fe}$ values on average indistinguishable from chondrites ($-0.01 \pm 0.01\%$; Craddock and Dauphas, 2011). Thus, Fe isotope fractionation during partial melting of the mantle was alternatively proposed to explain the difference in Fe isotope composition between mantle-derived basalts and chondrites (Weyer and Ionov, 2007; Teng et al., 2013), suggesting that complex processes invoked earlier (i.e., core formation or giant impact) may not be needed.

However, theoretical studies suggest that partial melting of mantle with chondritic value alone is insufficient to explain the observed MORB $\delta^{56}\text{Fe}$ values. Dauphas et al. (2009a) show that $\sim 10\%$ partial melting of mantle at $1200\text{ }^\circ\text{C}$ with a $\sim 0.3\%$ $\delta^{56}\text{Fe}$ fractionation between Fe^{2+} and Fe^{3+} and a melt with $\text{Fe}^{3+}/\sum\text{Fe}$ ratio of 0.16, corresponding to observed MORB (Bézos and Humler, 2005; Cottrell and Kelley, 2011), can only produce $\sim 0.04\%$ Fe isotope fractionation between MORB and their mantle source. Furthermore, using the synchrotron Nuclear Resonant Inelastic X-ray Scattering (NRIXS) techniques, Dauphas et al. (2014) measured the force constant of iron bonds in olivine as well as basaltic glasses and spinels synthesized under various oxygen fugacity conditions, and concluded that all these can only explain one-third of the difference in $\delta^{56}\text{Fe}$ values between MORB and the inferred mantle value ($0.02 \pm 0.03\%$; Weyer and Ionov, 2007). Uncertainties in model parameters used and some yet unidentified factors may account for the discrepancy between model predictions and observations. Alternatively, the observed $\delta^{56}\text{Fe}$ values of average MORB may not represent those of primary MORB melts.

While the majority of MORB preserve a near-homogeneous iron isotope composition (e.g., Teng et al., 2013), it has been argued that the complete range is more diverse than expected from a single-stage melting process, implying that the effect of source heterogeneity or magmatic evolution needs considering (Sossi et al., 2016). Based on the weak correlation between Fe isotopes and MgO in published MORB data, Sossi et al. (2016) argue that fractional crystallization may be important in causing Fe isotope fractionation during MORB evolution. Although these inferences are logical, they need testing. It should be noted that most previously studied MORB samples are from geo-

graphically dispersed, chemically diverse settings with a narrow compositional range (Weyer and Ionov, 2007; Teng et al., 2013; Nebel et al., 2015) (Table S1), which hampers evaluating the effect of fractional crystallization and mantle source heterogeneity on the observed Fe isotope compositions.

In this reason, we focus our Fe isotope study on a suite of well-characterized MORB lavas from the East Pacific Rise (EPR) axis at $10^\circ 30' \text{N}$ (Fig. 1). These samples are derived from a compositionally uniform source in terms of radiogenic isotopes and incompatible elements but span a wide compositional range in MgO (1.8–7.4 wt.%) with well-defined liquid lines of descent (LLD) (Regelous et al., 1999). They are thus best samples available for studying possible effect of magma evolution on Fe isotope fractionation at ocean ridges.

2. GEOLOGICAL BACKGROUND AND SAMPLES

The MORB samples were collected by dredging along a flowline across the East Pacific Rise (EPR) axis at $10^\circ 30' \text{N}$ (Fig. 1b, c) during the Phoenix 02 (R/V Melville) expedition (Batiza et al., 1996). Samples are from 40 dredges out to 50 km from the EPR axis on both the Pacific and Cocos Plates (Fig. 1c). Most off-axis samples were dredged from fault scarps, but closer to the ridge axis, an additional 30 samples were recovered by a rock-coring technique, which allowed more dense sampling (~ 2 samples/ km^2) of an area of $\sim 12\text{ km}^2$ within $\sim 3\text{ km}$ of the ridge axis (Regelous et al., 1999). The studied samples are fresh glasses (quenched melts) that span a large compositional range (e.g., MgO and SiO_2 ; Fig. 2), including basalts, basaltic andesites and andesites. They also display large variations in trace element concentrations, fully consistent with varying extents of fractional crystallization (Fig. S1) (Regelous et al., 1999). All the samples have Sr, Nd and Pb isotope compositions that are typical of Pacific MORB and have limited variations, reflecting their homogeneous mantle source (Regelous et al., 1999). No E-MORB were recovered at $10^\circ 30' \text{N}$, nor have any been dredged from the axis along this segment of the EPR. As some samples reported in Regelous et al. (1999) are no longer available, we thus select alternative samples from the same dredges. We have done new analysis of major and trace elements for these samples. Generally, samples from the same dredge have very similar compositions.

3. ANALYTICAL METHODS

3.1. Bulk rock Fe isotopes

Fresh MORB glass fragments were handpicked under a binocular microscope. Before digestion for trace element and isotope analysis, samples were cleaned with Milli-Q water for 10 min, three times, in an ultrasonic bath. The Sr-Nd-Fe isotopes were measured in the Laboratory of Ocean Lithosphere and Mantle Dynamics, Institute of Oceanology, Chinese Academy of Sciences (IOCAS). For Fe isotope analysis, about 5–10 mg of samples were digested with an acid mix of Lefort aqua regia (1HCl:

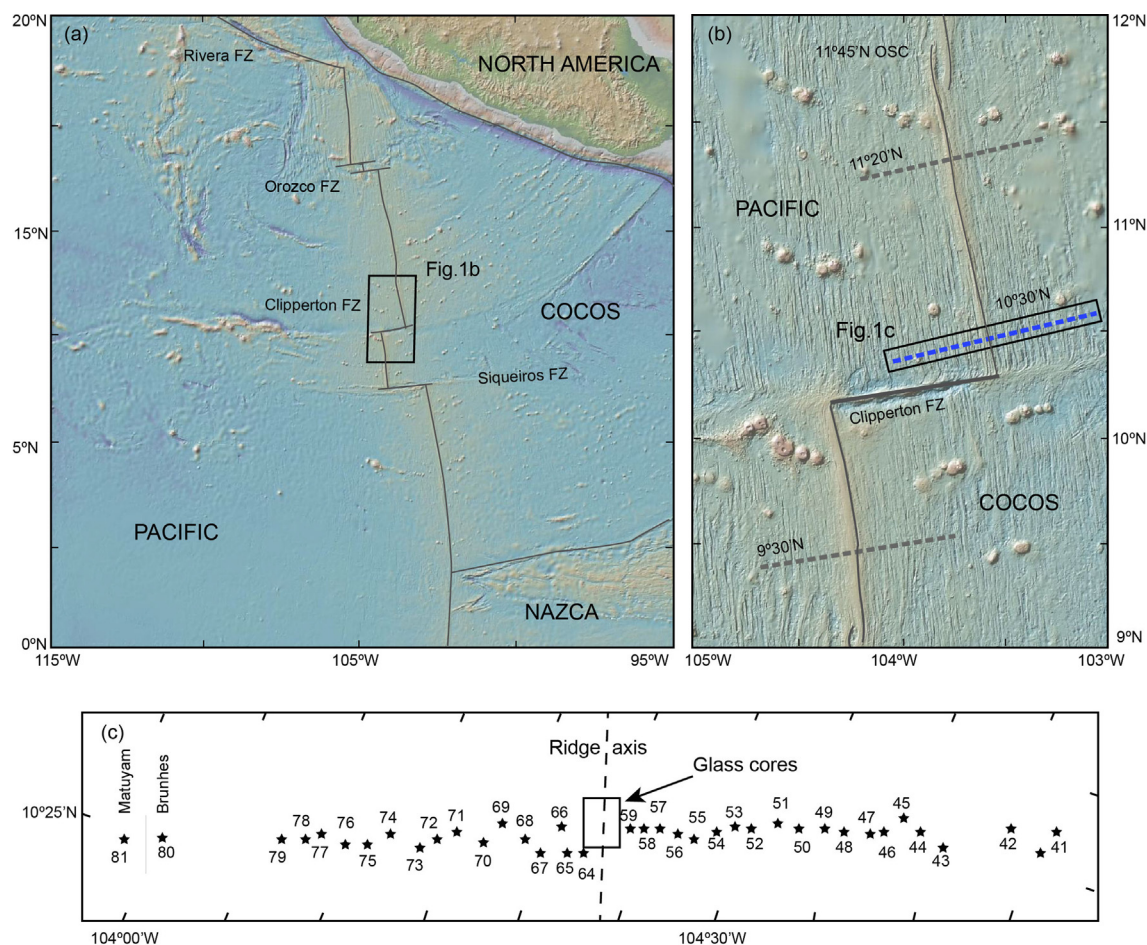


Fig. 1. (a) Simplified tectonic map of the northern EPR, indicating the study area. (b) Simplified tectonic map of the EPR between 9° and 12° N, showing the locations of the samples dredged/cored along flowlines across the EPR axis at 9°30'N, 10°30'N and 11°20'N during the Phoenix 02 expedition (Batiza et al., 1996). (c) Closeup positions of samples we study from the traverse at 10°30'N. Maps were generated in GeoMapApp (<http://www.geomapp.org/>). Plate boundaries and sample locations are after Regelous et al. (1999).

3HNO₃) and HF in a 15 ml PEFE beaker for 15 h, and then re-dissolved with distilled 3 mol L⁻¹ HNO₃ for two hours until complete dissolution after evaporation. Iron was subsequently purified with a polypropylene column filled with 1 ml AG-MP-1 M resin (200–400 mesh) in a HCl medium following the procedure in Sossi et al. (2015). After purification, each sample was doped with GSB Ni standard (an ultrapure single elemental standard solution from the China Iron and Steel Research Institute) as an internal mass bias monitor with Ni:Fe ratio of ~1.4:1. Iron isotopic compositions were determined by the “Ni doping” method using a Nu plasma II multiple collector–inductively coupled plasma–mass spectrometer (MC–ICP–MS) in wet plasma mode with medium resolution (a mass resolution > 7500). Mass bias fractionation during the analysis was corrected using ⁶⁰Ni/⁵⁸Ni similar to Zhu et al. (2018) with the ⁵⁸Fe interference on ⁵⁸Ni corrected based on ⁵⁶Fe. During analysis, every two sample solutions were bracketed with 14 ppm GSB Fe standard solution that was also doped with the GSB Ni solution with Ni:Fe ratio of ~1.4:1. The GSB Fe standard has been reported relative to IRMM014 ($\delta^{56}\text{Fe}_{\text{IRMM014}} = \delta^{56}\text{Fe}_{\text{GSB}} + 0.729$;

$\delta^{57}\text{Fe}_{\text{IRMM014}} = \delta^{57}\text{Fe}_{\text{GSB}} + 1.073$; He et al., 2015). Generally, isotopic compositions reported here are the averages of five repeated analyses. Iron isotopic composition are expressed in δ -notation and normalized to IRMM-014 value, i.e., $\delta^i\text{Fe} = [(^i\text{Fe}/^{54}\text{Fe})_{\text{sample}} / (^i\text{Fe}/^{54}\text{Fe})_{\text{IRMM-014}} - 1] \times 10^3$, where i refers to mass 56 or 57. The $\delta^{56}\text{Fe}$ values of the USGS standard BCR-2, AGV-2, BHVO-2 and W-2a were $0.07 \pm 0.04\text{‰}$ (2 s.d., $n = 9$), $0.09 \pm 0.06\text{‰}$ (2 s.d., $n = 10$), $0.08 \pm 0.05\text{‰}$ (2 s.d., $n = 17$), $0.04 \pm 0.06\text{‰}$ (2 s.d., $n = 11$), respectively, consistent with the literature values within error (Craddock and Dauphas, 2011; He et al., 2015; Sossi et al., 2015; McCoy-West et al., 2018).

For Sr–Nd isotopes, about 50 mg of each sample were digested with an acid mix of Lefort aqua regia (1HCl: 3HNO₃) and HF in a 15 ml PEFE beaker for 15 h, and then re-dissolved with distilled 3 mol L⁻¹ HNO₃ for 2 h until complete dissolution after evaporation. Sr were first separated by running through Sr-Spec resin. AG resin was then used to separate high field strength elements and rare earth elements (REEs). Nd was separated using Ln resin. The purified Sr and Nd were diluted for analysis with Nu plasma II MC–ICP–MS. The Sr and Nd isotope ratios were

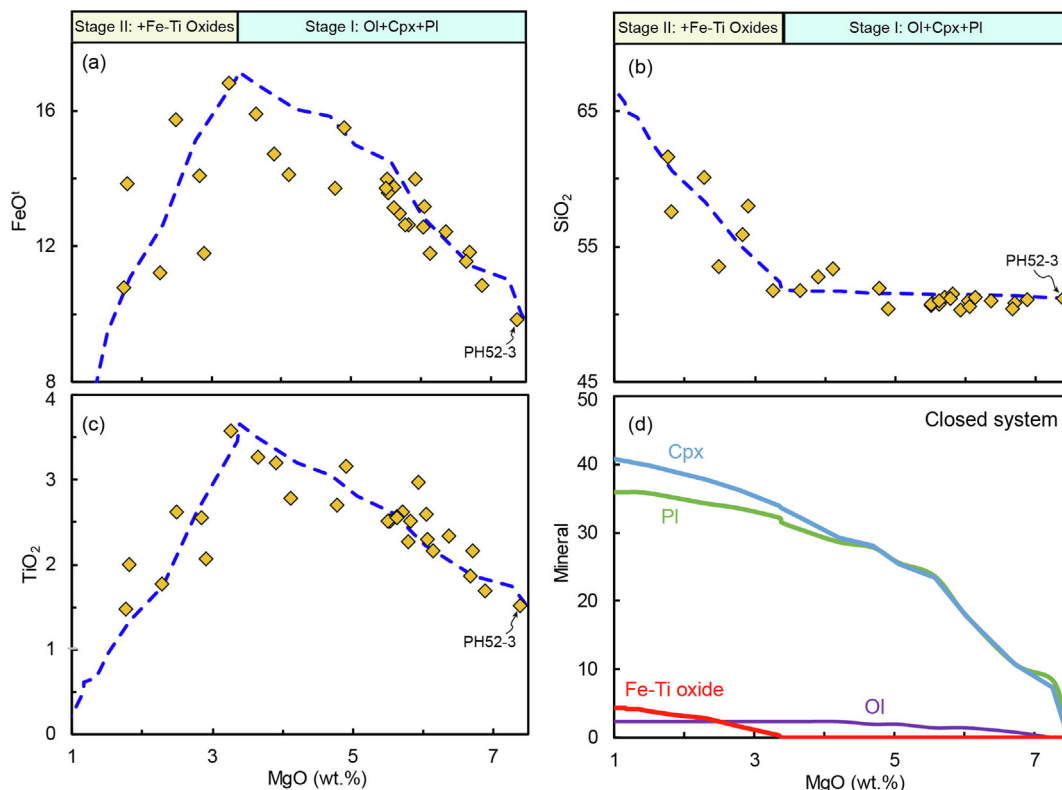


Fig. 2. (a–c) Plots of FeO^I , TiO_2 and SiO_2 vs. MgO for lavas from the EPR $10^\circ 30' \text{N}$ traverse we studied (diamonds). Liquid lines of descent shown are modeled using Petrolog3 (Danyushevsky and Plechov, 2011) with a starting composition of sample PH52-3, which fractionate olivine, clinopyroxene, and plagioclase at 2 kbar, using mineral melt models of Roeder and Emslie (1970) and Danyushevsky (2001), treating $\text{Fe}^{2+}/\text{Fe}^{3+}$ as a closed system (Danyushevsky and Plechov, 2011). The H_2O contents of the initial melt is assumed to be 0.05 wt.%. (d) Model results showing a primitive MORB melt (analog to PH-52-3) crystallizes olivine + clinopyroxene + plagioclase at Stage I until $\text{MgO} \approx 3.0$ wt. % when Fe-Ti oxides begin to crystallize at Stage II, which leads to rapid decrease of FeO^I , TiO_2 and increase of SiO_2 in the residual melt. Ol = olivine; Cpx = clinopyroxene; Pl = plagioclase.

normalized to $^{86}\text{Sr}/^{88}\text{Sr} = 0.1194$, $^{146}\text{Nd}/^{144}\text{Nd} = 0.7219$, respectively. Repeated analysis of NBS-987 and Jndi-1 Nd standard run during the same period of sample analysis yielded $^{87}\text{Sr}/^{86}\text{Sr} = 0.710250 \pm 22$ (2σ , $n = 9$) and $^{143}\text{Nd}/^{144}\text{Nd} = 0.512110 \pm 7$ (2σ , $n = 4$), respectively. Detailed methods for Sr-Nd elemental separation and isotope analysis are given by Sun et al. (2018).

The Sr-Nd-Fe isotopic data of the studied samples and rock standards are given in Table 1.

3.2. Glass major and trace elements

The major element, trace element and Sr-Nd-Pb isotopes of some samples from the EPR $10^\circ 30' \text{N}$ have been reported in Regelous et al. (1999). In addition, new major and trace elements for other samples are presented in Tables S2 and S3, respectively. The glass major elements were analyzed using electron probe microanalyzer using Cameca SX-50 at the University of Hawaii. To reduce systematic bias from different laboratories, we reanalyzed the trace elements for samples that had been previously studied (Regelous et al., 1999). The trace element analysis was done in the Laboratory of

Ocean Lithosphere and Mantle Dynamics, IOCAS, using ICP-MS (Agilent 7900) following Chen et al. (2017). The bulk-rock trace elements of USGS reference materials (Table S3) analyzed together with our samples agree well with reference values within error (Jochum et al., 2016).

4. RESULTS

The new major and trace elements data of the lavas from the EPR $10^\circ 30' \text{N}$ show that all the basalts and basaltic andesites samples with $\text{MgO} > 5$ wt.% have $[\text{La}/\text{Sm}]_N < 0.9$ and $\text{K}_2\text{O}/\text{TiO}_2 < 0.15$ and thus belong to N-MORB as reported by Regelous et al. (1999). In addition, the andesite samples have $[\text{La}/\text{Sm}]_N$ and $\text{K}_2\text{O}/\text{TiO}_2$ ratios of up to 1.0 and 0.6, respectively, as resulting from fractional crystallization (Regelous et al., 1999). The iron isotope data are given in Table 1 and are summarized in Fig. 3 together with the literature data for comparison. The $\delta^{56}\text{Fe}$ values of the EPR $10^\circ 30' \text{N}$ lavas range from +0.05 to +0.15‰, overlapping the literature MORB data (Weyer and Ionov, 2007; Teng et al., 2013; Nebel et al., 2015; Fig. 3).

Table 1
Sr-Nd-Fe isotopes of MORB glasses from East Pacific Rise at 10°30'N and rock standards.

Sample	MgO (wt.%)	$\delta^{56}\text{Fe}$ (‰)	2 s.d.	95% c.i.	$\delta^{57}\text{Fe}$ (‰)	2 s.d.	95% c.i.	N	$^{87}\text{Sr}/^{86}\text{Sr}$	$^{143}\text{Nd}/^{144}\text{Nd}$
MORB glasses from East Pacific Rise at 10°30'N										
PH43-2	1.81	0.12	0.02	0.01	0.18	0.06	0.04	5	0.702609 ± 10	0.513142 ± 6
PH45-2	3.25	0.10	0.05	0.03	0.17	0.03	0.02	5	0.702644 ± 10	0.513147 ± 6
Replicated		0.09	0.02	0.01	0.13	0.05	0.02	6		
PH49-2	4.78	0.11	0.04	0.03	0.22	0.06	0.04	5		
PH51-6	5.70	0.08	0.03	0.02	0.13	0.03	0.02	5		
PH52-3	7.38	0.06	0.04	0.02	0.09	0.06	0.03	6		
Replicated		0.05	0.06	0.02	0.07	0.08	0.03	11		
PH54-1	6.87	0.05	0.04	0.02	0.09	0.07	0.05	5	0.702538 ± 10	0.513163 ± 6
PH55-1	6.36	0.06	0.03	0.02	0.11	0.08	0.05	5		
PH56-3	6.71	0.10	0.04	0.03	0.13	0.09	0.05	5		
PH59-1	6.04	0.09	0.04	0.02	0.19	0.06	0.02	10		
PH60-6	4.90	0.11	0.02	0.01	0.13	0.03	0.02	5	0.702571 ± 12	0.513147 ± 6
PH62-4	6.13	0.12	0.02	0.01	0.15	0.02	0.01	5		
PH63-1*	5.62	0.10	0.02	0.02	0.14	0.07	0.04	5	0.702546 ± 9	
PH64-2*	5.51	0.10	0.04	0.02	0.15	0.04	0.03	5	0.702536 ± 9	0.513140 ± 6
PH65-1*	5.53	0.09	0.01	0.01	0.13	0.03	0.02	5	0.702531 ± 9	0.513158 ± 7
PH66-1	5.92	0.11	0.02	0.01	0.21	0.05	0.03	5	0.702600 ± 12	0.513158 ± 6
PH69-3	6.66	0.07	0.03	0.02	0.09	0.04	0.02	5		
Replicated		0.09	0.04	0.02	0.12	0.06	0.04	5		
PH71-7	6.06	0.06	0.02	0.01	0.11	0.04	0.02	5		
PH75-1	3.64	0.10	0.03	0.02	0.11	0.07	0.04	5		
PH76-3*	2.49	0.12	0.02	0.01	0.18	0.02	0.01	5	0.702530 ± 9	0.513161 ± 7
PH77-7	5.82	0.07	0.01	0.01	0.13	0.04	0.02	5	0.702586 ± 12	0.513158 ± 8
PH78-1*	2.83	0.10	0.02	0.01	0.13	0.02	0.01	5	0.702568 ± 9	0.513166 ± 7
PH78-2*	3.90	0.12	0.03	0.02	0.15	0.04	0.03	5	0.702549 ± 9	0.513155 ± 8
PH78-5	4.11	0.09	0.01	0.01	0.17	0.01	0.01	5	0.702566 ± 9	0.513172 ± 7
PH79-1	2.90	0.15	0.03	0.02	0.25	0.04	0.03	4	0.702592 ± 9	0.513157 ± 7
PH79-3	1.76	0.12	0.03	0.02	0.16	0.06	0.04	5		
PH79-5	2.27	0.08	0.02	0.01	0.14	0.03	0.02	6		
PHGC-74*	5.50	0.10	0.03	0.01	0.15	0.04	0.02	6	0.702559 ± 9	0.513140 ± 7
PHGC-78	5.79	0.10	0.03	0.02	0.18	0.06	0.03	5		
PHGC-83	5.62	0.06	0.02	0.01	0.07	0.04	0.02	6		
Rock standards										
BCR-2		0.07	0.04	0.01	0.12	0.04	0.01	9	0.705040 ± 8	0.512634 ± 6
AGV-2		0.09	0.06	0.02	0.14	0.09	0.03	10	0.704010 ± 8	0.512779 ± 4
BHVO-2		0.08	0.05	0.01	0.12	0.11	0.03	17		
W-2a		0.04	0.06	0.02	0.07	0.09	0.03	11		

Replicated analyses are for newly digested samples. To represent measurement uncertainty both the two-standard deviation (2 s.d.) and 95% confidence interval (c.i.) of the mean for N replicate analyses of the same solution are presented. MgO and Sr-Nd isotopes data of samples marked with asterisks is from [Regelous et al. \(1999\)](#), others are from this study. Error for Sr-Nd isotopes is two-standard errors for the final digits.

5. DISCUSSION

5.1. Statistical tests for the Fe isotopic composition of MORB: homogeneous or heterogeneous?

The extensive survey of the high precision Fe isotopic composition of global MORB by [Teng et al. \(2013\)](#) is an important observation, which suggests that the majority of MORB have near-homogeneous $\delta^{56}\text{Fe}$ values of $+0.105 \pm 0.006\text{‰}$ (2 s.e., $n = 43$). However, examination of the literature MORB data (Table S1) shows that MORB are likely to be heterogeneous with a relatively wide range of $\delta^{56}\text{Fe}$ from 0.06 to 0.18‰ as observed by [Sossi et al. \(2016\)](#), although they span a relatively narrow range in $\text{Mg}^\#$ [$\text{Mg}/(\text{Mg} + \text{Fe}^{2+}) \times 100$] (45–72). We use statistical methods to test the extent to which the observed scatter

in the literature MORB data using reduced χ^2 (or MSWD, Mean Square Weighted Deviation) values, similar to that of [Dauphas et al. \(2009b\)](#) and [Teng et al. \(2013\)](#). The calculations are listed in [Table 2](#).

The calculated MSWD value is 7.6 for the literature MORB data ($n = 55$), which is outside the 95% confidence interval of 0.7–1.4 for $n - 1 = 54$ degree of freedom. If samples from our study included, the calculated MSWD is 8.1 ($n = 84$), which is also outside the 95% confidence interval of 0.7–1.3 for $n - 1 = 83$ degree of freedom. Thus, the dispersion in the MORB $\delta^{56}\text{Fe}$ values cannot be explained by the analytical uncertainties of the individual data points. Although one cannot totally exclude inter-laboratory bias because of lacking comparable geological reference standards in the literature, it is more likely that MORB are heterogeneous in Fe isotopes, because (1) from single labo-

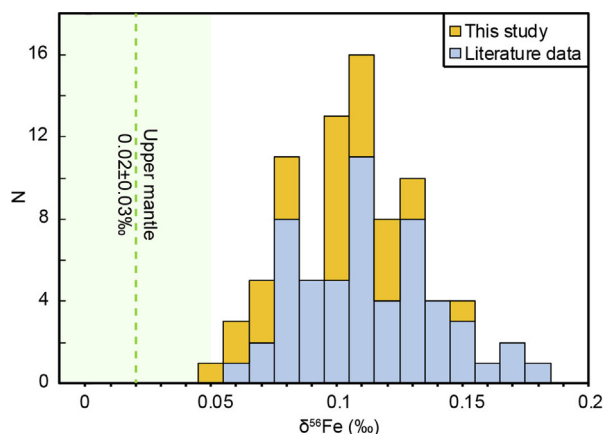


Fig. 3. Histogram of our Fe isotopic data on lavas from the EPR 10°30'N traverse, compared with the literature MORB data (Table S1) (Weyer and Ionov, 2007; Teng et al., 2013; Nebel et al., 2015). The black vertical solid line represents the Fe isotopic composition of the upper mantle ($\delta^{56}\text{Fe} = +0.02 \pm 0.03\text{‰}$, Weyer and Ionov, 2007; Dauphas et al., 2009a, 2009b).

ratory perspective, while MORB samples span a narrow range in $\text{Mg}^\#$ (0.48–0.67), the calculated MSWD value from Teng et al. (2013) is 1.9, also outside the 95% confidence interval of 0.6–1.5 for $n - 1 = 42$ degree of freedom; (2) in the case of our study, the MSWD of lavas from EPR 10°30'N is 3.8 ($n = 29$). This value is outside the 95% confidence interval of 0.5–1.6 for $n - 1 = 28$ degree of freedom. It has been suggested that a single stage melting process cannot explain the complete $\delta^{56}\text{Fe}$ range of all MORB data (Sossi et al., 2016), indicating that mantle source heterogeneity and/or magma evolution may play an important role in causing the variation of MORB Fe isotopes.

5.2. The origin of Fe isotope variation of lavas from EPR 10°30'N

5.2.1. Mantle source heterogeneity

It has been suggested that mantle metasomatism can modify Fe isotopic composition of mantle material (Williams et al., 2005; Weyer and Ionov, 2007). For example, mantle peridotites show highly varied Fe isotope compositions, extending either towards increasingly heavy or to extremely light values with increasing enrichments in iron, which was interpreted by melt infiltration and kinetic Fe isotope fractionation associated with diffusion during melt

percolation (Weyer and Ionov, 2007). Similarly, Williams and Bizimis (2014) found that the range of $\delta^{56}\text{Fe}$ variations measured in peridotites cannot be explained by a simple partial melting model because the most depleted peridotites have only experienced $\sim 10\%$ melt extraction, which would be insufficient to impart large isotope fractionation to the residue (the iron solid/melt partition coefficient is ~ 1). They also argued that the published $\delta^{56}\text{Fe}$ data on mantle melting products, such as MORB and OIB, show variation greater than predicted by melting from a $\delta^{56}\text{Fe}$ -homogeneous mantle (Williams and Bizimis, 2014). They thus conclude that the mantle may be heterogeneous in its Fe isotopic composition, mirroring the distribution of pyroxenitic *versus* peridotitic sources (Williams and Bizimis, 2014). Such mantle heterogeneity may be observed in lavas in mantle-plume basalts, as previously reported on samples from the Society, Cook-Austral and Samoan islands (Teng et al., 2013; Konter et al., 2016). However, source heterogeneity is not likely the cause for the Fe isotopic variation in our study here, because (1) lavas from the EPR 10°30'N show uniform mantle source composition in terms of Sr-Nd-Pb isotopes (Reglous et al., 1999); (2) $\delta^{56}\text{Fe}$ does not vary with indicators of source enrichment, such as $\text{K}_2\text{O}/\text{TiO}_2$, $^{87}\text{Sr}/^{86}\text{Sr}$ and $^{143}\text{Nd}/^{144}\text{Nd}$ (Fig. 4). Notably the high $\text{K}_2\text{O}/\text{TiO}_2$ lavas are those highly evolved ones with low MgO, TiO_2 , FeO and high SiO_2 (Fig. 2).

5.2.2. Magma differentiation

The removal of minerals with Fe isotope compositions distinct from their host magmas has been proposed to explain Fe isotope fractionation of igneous rocks (Teng et al., 2008; Schuessler et al., 2009; Sossi et al., 2012; Telus et al., 2012; Foden et al., 2015; McCoy-West et al., 2018; Peters et al., 2019). For example, Kilauea Iki lavas (Hawaii) show increasing $\delta^{56}\text{Fe}$ values with decreasing MgO, starting from basalts with ~ 11 wt.% MgO and $\sim 0.1\text{‰}$ $\delta^{56}\text{Fe}$ values to andesitic compositions with $\sim 3\%$ MgO and $\sim 0.2\text{‰}$ $\delta^{56}\text{Fe}$ (Fig. 5; Teng et al., 2008). The Red Hill intrusion (Tasmania) also displays a systematic increase of $\delta^{56}\text{Fe}$ with magmatic differentiation when $\text{MgO} > 1$ wt.% (Fig. 5). However, it shows abrupt decrease in $\delta^{56}\text{Fe}$ below 1 wt.% MgO, a point coincident with the rapid depletion of FeO^t (Sossi et al., 2012). Despite a compositional gap for the “turning point”, the oceanic island basalts (OIB) from the Society Islands show similar trend to Red Hill intrusion (Fig. 5; Teng et al., 2013). The increasing $\delta^{56}\text{Fe}$ values with magma differentiation in Kilauea Iki, Red Hill and Society Islands samples have been explained

Table 2

Calculated reduced χ^2 (MSWD) and 95% confidence interval for MORB from literature and this study.

Data source	N	Mean $\delta^{56}\text{Fe}$ (‰)	2 s.e. (‰)	MSWD	95% c.i.	
					Lower	Upper
Literature MORB*	55	0.109	0.008	7.6	0.7	1.4
All MORB [#]	84	0.104	0.006	8.1	0.7	1.3
MORB (Teng et al., 2013)	43	0.105	0.006	1.9	0.6	1.5
MORB (This study)	29	0.094	0.008	3.8	0.5	1.6

* Literature MORB data are from Weyer and Ionov (2007), Teng et al. (2013) and Nebel et al. (2015).

[#] All MORB data is from above literature and this study.

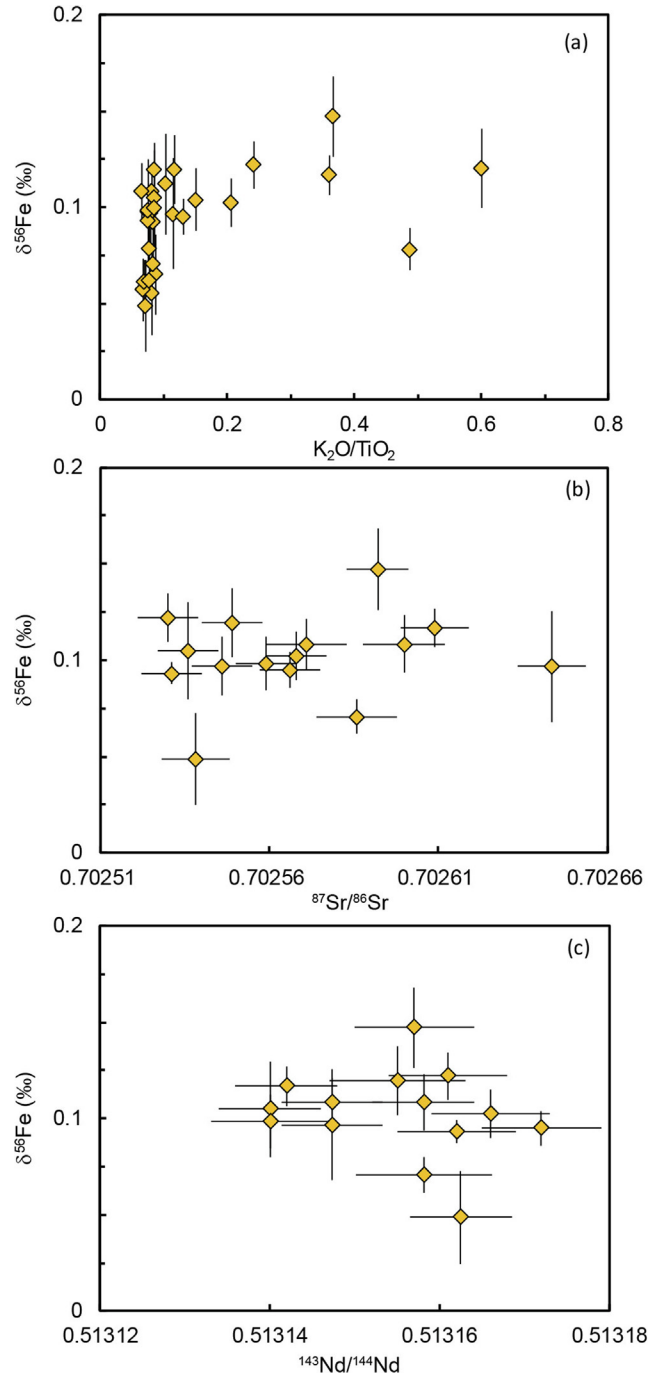


Fig. 4. Plot of $\delta^{56}\text{Fe}$ vs. $\text{K}_2\text{O}/\text{TiO}_2$ (a), $^{87}\text{Sr}/^{86}\text{Sr}$ (b) and $^{143}\text{Nd}/^{144}\text{Nd}$ (c) for lavas from the EPR 10°30'N traverse. Throughout this paper error bars of $\delta^{56}\text{Fe}$ on individual points are the 95% c.i. on that sample. Error bars of Sr and Nd isotopes are 2 s.e.

with fractional crystallization of Fe^{3+} -poor phases (olivine, pyroxene) in a closed system (Teng et al., 2008; 2013; Sossi et al., 2012), whereas decrease in $\delta^{56}\text{Fe}$ in the latter stages was interpreted as resulting from crystallization removal of heavy Fe-bearing oxide minerals (Sossi et al., 2012; Teng et al., 2013). These explanations provide a causal relationship between Fe isotope and major element data.

Lavas from the EPR 10°30'N in this study show trend of $\delta^{56}\text{Fe}$ against MgO somewhat similar to Red Hill and

Society Islands data (Fig. 5). As shown in Fig. 5, $\delta^{56}\text{Fe}$ initially displays a systematic increase with falling MgO, then slightly decrease in $\delta^{56}\text{Fe}$ below ~ 3 wt% MgO (Stage I), which is also coincident with the rapid depletion of FeO^t and TiO_2 (Stage II). As previously suggested, large variations in major and trace element concentrations in lavas from the EPR 10°30'N result from large extents of fractional crystallization (Regelous et al., 1999). In order to match the observed major element variations for the

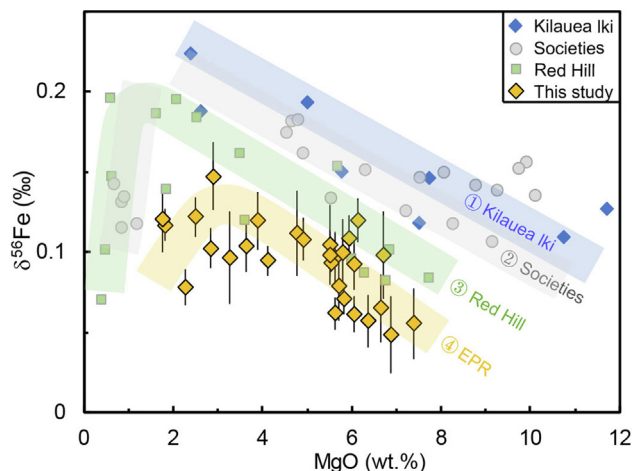


Fig. 5. Plot of $\delta^{56}\text{Fe}$ vs. MgO for lavas from the EPR $10^{\circ}30'\text{N}$ traverse. For comparison, data from Kilauea Iki (Teng et al., 2008), Societies (Teng et al., 2013), and Red Hill (Sossi et al., 2012) are also plotted. The colored bands indicate trends of $\delta^{56}\text{Fe}$ variation with magma differentiation (decreasing MgO).

samples in this study, we explore the fractional crystallization models using Petrolog3 software (Danyushevsky and Plechov, 2011) with a starting composition of sample PH52-3. As illustrated in Fig. 2, crystallization of olivine, clinopyroxene and plagioclase results in increase of FeO^{t} and TiO_2 values and decrease of MgO value in the remaining melt at Stage I until Fe-Ti oxide begins to crystallize at Stage II, which leads to decrease in FeO^{t} and TiO_2 with decreasing MgO in the remaining melts.

The above model may also explain their Fe isotopic variation, which can be approximated with a Rayleigh fractionation model (Fig. 6, grey curves), using the following equation:

$$\delta^{56}\text{Fe}_{\text{melt}} = \delta^{56}\text{Fe}_{\text{melt0}} + \Delta^{56}\text{Fe}_{\text{crystal-melt}} \times \ln(f_{\text{Fe}}) \quad (1)$$

where $\delta^{56}\text{Fe}_{\text{melt}}$ and $\delta^{56}\text{Fe}_{\text{melt0}}$ refer to $\delta^{56}\text{Fe}$ values of residual and initial melt, respectively; $\Delta^{56}\text{Fe}_{\text{crystal-melt}}$ ($\Delta^{56}\text{Fe}_{\text{X-Y}} = \delta^{56}\text{Fe}_{\text{X}} - \delta^{56}\text{Fe}_{\text{Y}}$) represents Fe isotope fractionation between the crystallized mineral assemblage and melt; f_{Fe} is the fraction of Fe remaining in the melt, which can be calculated by $f_{\text{Fe}} = F \times C_{\text{melt,FeO}}/C_{\text{melt0,FeO}}$ ($C_{\text{melt,FeO}}$ and $C_{\text{melt0,FeO}}$ refer to FeO^{t} content in residual and initial melt, respectively). F is the fraction of melt remaining. As shown in Fig. 6, the trend of $\delta^{56}\text{Fe}$ vs. MgO of the EPR $10^{\circ}30'\text{N}$ lavas at Stage I can be well modeled by olivine gabbroic fractionation with a fractionation factor of

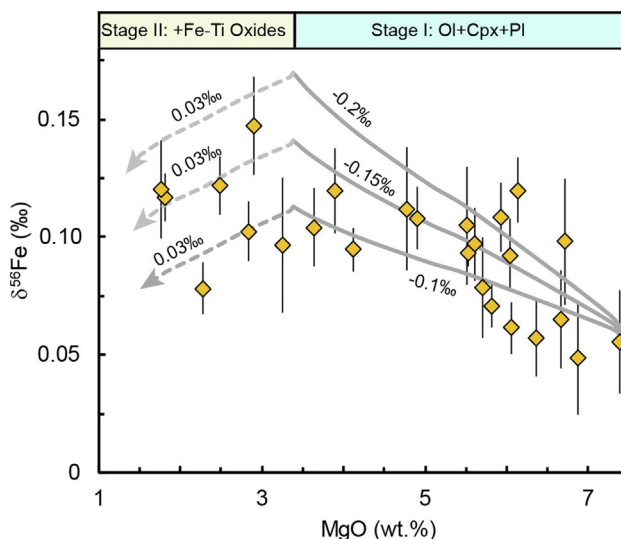


Fig. 6. Modeling of $\delta^{56}\text{Fe}$ variation with magma differentiation indicator of MgO using model results in Fig. 2. Stage I: the solid grey lines represent calculated Fe isotopic compositions of residual melts during fractional crystallization of olivine, clinopyroxene and plagioclase by assuming a Rayleigh distillation process with average crystal-melt fractionation factors ($\Delta^{56}\text{Fe}_{\text{crystal-melt}}$) of -0.1‰ , -0.15‰ and -0.2‰ (See text for the detailed calculations). Stage II: the dashed grey lines represent Fe isotopic variations of residual melts as the result of Fe-Ti oxide crystallization with $\Delta^{56}\text{Fe}_{\text{crystal-melt}}$ of 0.03‰ . Ol = olivine; Cpx = clinopyroxene; Pl = plagioclase.

$\Delta^{56}\text{Fe}_{\text{crystal-melt}}$ of -0.1 to -0.2% , similar to fractionation factors found to account for the isotopic variation during differentiation of Kilauea Iki (Teng et al., 2008) and Red Hill (Sossi et al., 2012).

At stage II, crystallization of Fe-Ti oxides, i.e., complex solid solutions of magnetite and ilmenite, results in decreasing FeO^1 and TiO_2 with decreasing MgO (Fig. 2). It has been suggested that crystallization of magnetite or ilmenite from melt alone could dramatically lower or enhance $\delta^{56}\text{Fe}$ of the residual melt (Sossi et al., 2012; Dauphas et al., 2017; Cao et al., 2019). A recent study for Fe isotopic compositions of whole rocks and mineral separates in the Panzihua mafic layered intrusion shows that magnetite separates have a strikingly complementary trend with the coexisting ilmenite separates in $\delta^{56}\text{Fe}$ values, yet the calculated bulk Fe-Ti oxides (magnetite + ilmenite) has a small range of $\delta^{56}\text{Fe}$, identical to those for the whole rock Fe isotope compositions (Cao et al., 2019). Their further models indicate that the effect of crystallization of Fe-Ti oxides on Fe isotopes is controlled by magnetite/ilmenite ratios (Cao et al., 2019). As observed in Fig. 6, lavas from the EPR 10°30'N in this study slightly decrease in $\delta^{56}\text{Fe}$ at Stage II, which can be well reproduced by a fractionation factor of $\Delta^{56}\text{Fe}_{\text{Fe-Ti oxide-melt}}$ of $\sim 0.03\%$. If we adopt ilmenite-melt fractionation factor ($\Delta^{56}\text{Fe}_{\text{Ilmenite-melt}}$) of -0.09% and magnetite-melt fractionation factor ($\Delta^{56}\text{Fe}_{\text{Magnetite-melt}}$) of 0.14% , same as model parameters used by Cao et al. (2019), we can obtain magnetite/ilmenite ratios of ~ 0.5 .

5.3. The Fe isotope composition of primary melts parental to lavas from EPR 10°30'N

As discussed above, the Fe isotope composition of MORB can be fractionated during magma differentiation. It is thus incorrect to use variably evolved MORB melts to estimate the Fe isotope compositions of their primary melts and mantle sources. It has been suggested that MORB melts corrected to $\text{Mg}^\# = 72$ are in equilibrium with mantle olivine of Fo_{90} (Niu and O'Hara, 2008; Niu, 2016). Using a single set of correction coefficients applicable to the global MORB dataset (Niu and O'Hara, 2008), we can obtain the major elements of primary melt for the EPR 10°30'N lavas using samples with $\text{MgO} \geq 6.5$ wt.% (less evolved), e.g., $\text{Mg}_{72} = 9.91 \pm 0.09$ wt.% ($\pm 1\text{SD}$), $\text{Fe}_{72} = 7.7 \pm 0.14$ wt.% ($\pm 1\text{SD}$). Accordingly, we can estimate the Fe isotopic composition of primary melts for the EPR 10°30'N lavas.

We use similar models (Eq. (1)) in Section 5.2.2 and parameters (Table S4) to back-calculate $\delta^{56}\text{Fe}$ of the primary melt by following equations.

$$C_{\text{melt,MgO}} = C_{\text{primary melt,MgO}} \times F^{(D_{\text{MgO}} - 1)} \quad (2)$$

$$f_{\text{Fe}} = F \times C_{\text{melt,FeO}} / C_{\text{primary melt,FeO}} \quad (3)$$

$$\delta^{56}\text{Fe}_{\text{primary melt}} = \delta^{56}\text{Fe}_{\text{melt}} - \Delta^{56}\text{Fe}_{\text{crystal-melt}} \times \ln(f_{\text{Fe}}) \quad (4)$$

where $\delta^{56}\text{Fe}_{\text{melt}}$ and $\delta^{56}\text{Fe}_{\text{primary melt}}$ refer to $\delta^{56}\text{Fe}$ values of residual melt and primary melt values, respectively; $\Delta^{56}\text{Fe}_{\text{crystal-melt}}$ represents Fe isotope fractionation between the crystallized mineral assemblage and melt; $C_{\text{melt, MgO}}$

and $C_{\text{primary melt,MgO}}$ refer to MgO content in residual and initial melt, respectively; D_{MgO} is partition coefficient of MgO between crystal and melt; f_{Fe} is the fraction of Fe remaining in the melt; F is the fraction of melt remaining.

With Eqs. (2)–(4) combined, we have,

$$\delta^{56}\text{Fe}_{\text{primary melt}} = \delta^{56}\text{Fe}_{\text{melt}} - \Delta^{56}\text{Fe}_{\text{crystal-melt}} \times \left[\frac{\ln\left(\frac{C_{\text{melt,MgO}}}{C_{\text{primary melt,MgO}}}\right)}{D_{\text{MgO}} - 1} + \ln\left(\frac{C_{\text{melt,FeO}}}{C_{\text{primary melt,FeO}}}\right) \right] \quad (5)$$

Here, we estimate the magnitude of $\Delta^{56}\text{Fe}_{\text{crystal-melt}} \approx -0.15\%$ from the trend of the our samples (see Fig. 5), a value consistent with that reported for studies of other mafic igneous systems (Teng et al., 2008; Sossi et al., 2012, 2016). To avoid effects of magnetite fractionation, we only use samples with $\text{MgO} > 4.0$ wt.% to estimate the Fe isotopic composition of primary melt for EPR 10°30'N lavas using Eq. (5).

The $\delta^{56}\text{Fe}$ values of estimated primary melts of EPR 10°30'N lavas is $0.04 \pm 0.01\%$ (2 s.e.), which is consistent with corrected value of $\delta^{56}\text{Fe}$ values ($0.03 \pm 0.01\%$, 2 s.e., $n = 20$) for our samples with $\text{MgO} > 4.0$ wt.% by applying a correction method by Sossi et al. (2016) (see Sossi et al., 2016 for a detailed outline). Notably, this value of primary melt of EPR 10°30'N lavas is similar to the corrected primary N-MORB values ($\delta^{56}\text{Fe} = 0.067$, derived from $\delta^{57}\text{Fe}$) by Sossi et al. (2016). It appears to be lower than published average MORB ($\delta^{56}\text{Fe} = +0.105 \pm 0.006\%$, 2 s. e.; Teng et al., 2013), but slightly higher than that of chondrite and mantle peridotite (Weyer and Ionov, 2007).

Dauphas et al. (2014) measured the force constant of iron bonds using the NRIXS synchrotron techniques in olivine as well as basaltic magmas. They used these new force constant results in a model of Fe isotope fractionation during partial melting and found that MORB melt generated by 10% partial melting of mantle peridotite with $\text{Fe}^{3+}/\text{Fe}^{\text{tot}}$ would have $\delta^{56}\text{Fe}$ values that are fractionated by $+0.023 \pm 0.020\%$ relative to their source rocks (Dauphas et al., 2014). If we assume a mantle source composition of $\delta^{56}\text{Fe} = +0.02 \pm 0.03\%$ (Weyer and Ionov, 2007) as a starting point (similar to Weyer and Ionov, 2007; Dauphas et al., 2009a, 2009b; Craddock et al., 2013), partial melting can well reproduce the estimated primary melt of lavas from the EPR 10°30'N as well as the estimated primary melt ($\delta^{56}\text{Fe} = 0.067\%$) of global MORB by Sossi et al. (2016).

5.4. Comparison with available MORB and OIB data

Compared to OIB data on samples from Kilauea Iki and Society Islands (Teng et al., 2013), the $\delta^{56}\text{Fe}$ values of the EPR 10°30'N lavas are much lower at a given MgO (Fig. 5) or $\text{Mg}^\#$ (not shown), which most likely reflects that the mantle source of EPR 10°30'N lavas is more depleted in heavy Fe. In addition, from a global perspective, some published MORB data, especially E-MORB, also have heavier Fe isotopes (Fig. 7). As per the partial melting model by Dauphas et al. (2014), 10% melting of chondrite-like mantle

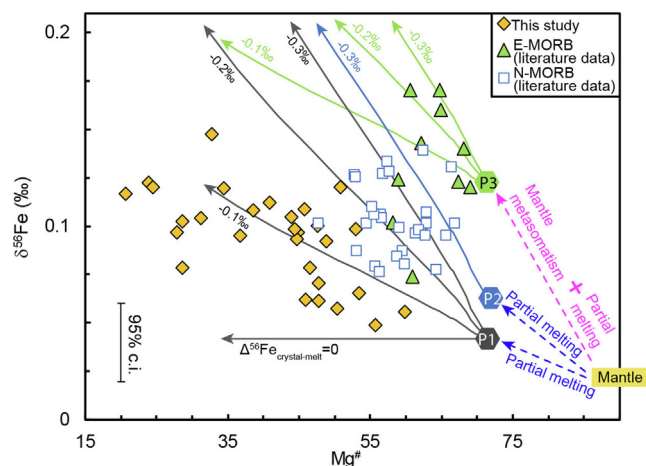


Fig. 7. Models illustrate potential generation of global MORB $\delta^{56}\text{Fe}$ values because of varying sources and processes. $\sim 10\%$ and $\sim 0.1\%$ degree of partial melting of upper mantle with $\delta^{56}\text{Fe}$ of 0.02‰ can generate primary melt with $\delta^{56}\text{Fe}$ of $\sim 0.04\text{‰}$ (P1) and $\sim 0.06\text{‰}$ (P2), respectively. Partial melting of metasomatized mantle can generate primary melt with high $\delta^{56}\text{Fe}$ of $\sim 0.14\text{‰}$ (P3) (cf. Konter et al., 2016). The solid lines with arrows represent the variation of $\delta^{56}\text{Fe}$ vs. $\text{Mg}^\#$ of the residual melt as a result of fractional crystallization of primary melt P1, P2 and P3. The fractionation factors are chosen to vary from -0.1 to -0.3‰ . The major elements of primary melts for EPR $10^\circ 30' \text{N}$ lavas are $\text{Mg}_{72} = 9.91 \pm 0.09$ wt.% ($\pm \text{SD}$), $\text{Fe}_{72} = 7.7 \pm 0.14$ wt.% ($\pm \text{SD}$), $\text{Al}_{72} = 16.44 \pm 0.18$ wt.% ($\pm \text{SD}$), $\text{Ti}_{72} = 1.15 \pm 0.16$ wt.% ($\pm \text{SD}$), $\text{Si}_{72} = 50.44 \pm 0.25$ wt.% ($\pm \text{SD}$), $\text{Ca}_{72} = 11.19 \pm 0.17$ wt.% ($\pm \text{SD}$), $\text{Na}_{72} = 2.28 \pm 0.10$ wt.% ($\pm \text{SD}$), $\text{K}_{72} = 0.06 \pm 0.02$ wt.% ($\pm \text{SD}$), $\text{P}_{72} = 0.12 \pm 0.03$ wt.% ($\pm \text{SD}$), calculated using method described in Niu and O'Hara (2008) based on samples with $\text{MgO} \geq 6.5$ wt.%. In this method, they obtained a set of polynomial regression coefficients for each oxide based on the entire global dataset and project each sample along the polynomial curves to $\text{Mg}^\# = 72$ (Niu et al., 1999; Niu and O'Hara, 2008). The fractional crystallization models, conditions, H_2O content and other parameters are the same as for models (Fig. 2) in Section 5.2.2 but for higher pressure (4 kbar). The representative sample uncertainty is $\pm 95\%$ c.i. from replicate analyses of W-2a.

can produce primary melt with $\delta^{56}\text{Fe}$ of $\sim 0.04\text{‰}$ (P1 in Fig. 7) and even very low degree ($\sim 0.1\%$) melting of mantle can only generate primary melt with $\delta^{56}\text{Fe}$ of $\sim 0.06\text{‰}$ (P2 in Fig. 7), both of which are lower than that of average MORB. With these model $\delta^{56}\text{Fe}$ values of primary melt, we can further explore the effect of fractional crystallization (see Fig. 2) on Fe isotope. The major elements of the primary melt are estimated from lavas from the EPR $10^\circ 30' \text{N}$ (see above). As illustrated in Fig. 7, the isotopically light primary melt (P1) can well reproduce the trend of $\delta^{56}\text{Fe}$ vs. $\text{Mg}^\#$ of the EPR $10^\circ 30' \text{N}$ lavas with fractionation factors of $\Delta^{56}\text{Fe}_{\text{crystal-melt}}$ of -0.1 to -0.2‰ through magma differentiation. The isotopically heavy primary melt (P2) with even the most extreme fractionation factor (-0.3‰) cannot explain the elevated $\delta^{56}\text{Fe}$ values of some E-MORB, indicating that processes other than fractional crystallization may also affect the Fe isotopic composition of global MORB, such as mantle heterogeneity resulting from mantle metasomatism as discussed above (Section 5.2.1), which can elevate the $\delta^{56}\text{Fe}$ mantle source values (Weyer and Ionov, 2007; Williams and Bizimis, 2014; Konter et al., 2016). For example, Samoan metasomatized peridotites have $\delta^{56}\text{Fe}$ value up to 0.07‰ and models show that partial melting of such metasomatized mantle with high $\text{Fe}^{3+}/\text{Fe}^{2+}$ might generate melt with high $\delta^{56}\text{Fe}$ value of $\sim 0.14\text{‰}$ (P3) (Konter et al., 2016). An analogous calculation shows that fractional crystallization of a similar, high $\delta^{56}\text{Fe}$ parental magma with fractionation factors of $\Delta^{56}\text{Fe}_{\text{crystal-melt}}$ of -0.1 to -0.3‰ can reproduce melts with $\delta^{56}\text{Fe}$ values similar to the higher value of some E-MORB (Fig. 7). Thus, although fractional crystallization can well

explain the Fe isotopic variation of lavas from the EPR $10^\circ 30' \text{N}$, a combination of processes is required to generate global MORB data.

5.5. Implications for the Fe isotope composition of the Earth

About 90% of Earth's Fe is in the core (McDonough, 2014), thus if there were any Fe isotope fractionation between metal and silicate during core formation, this would significantly fractionate Fe isotopes in Earth's mantle. However, there has been significant debate over whether core-mantle separation leads to Fe isotope fractionation (Poitrasson et al., 2009; Hin et al., 2012; Shahar et al., 2015; Liu et al., 2017; Elardo et al., 2019). The largest fractionation between metal and silicate ($\Delta^{56}\text{Fe}_{\text{metal-silicate}}$) reported by Shahar et al. (2015) is $-0.08 \pm 0.03\text{‰}$ at 1–2 GPa and 1650 °C. This P-T condition is much lower than required for the core formation at $\sim 40\text{--}60$ GPa and ~ 3000 K (Siebert et al., 2013). In contrast, Poitrasson et al. (2009) and Hin et al. (2012) suggested that fractionation was not resolvable between metal and silicate in their experiments. Similarly, based on extensive NRIXS study, Liu et al. (2017) again found no significant difference in iron isotope fractionation between pure iron metal and iron alloyed with ~ 16 wt % S at all pressures. Therefore, it seems that the fractionation between silicate and metal at conditions relevant to the core formation may be small, but more rigorous work is needed, both experimental and theoretical simulation, to place constraints on possible Fe isotope fractionation during processes of core formation.

MORB are the most abundant igneous rocks on the Earth as they cover much of the global ocean floor and continue to form along the ~60,000 km long globe-encircling ocean ridges (Crisp, 1984; Niu, 2016). Therefore, MORB can provide insights into the Fe isotopic composition of the Earth's mantle. However, it should be noted that actual MORB melts display huge compositional variations in contrast to the widely referenced average N- and E-MORB due to MORB melt evolution (see Niu and O'Hara, 2009). Thus, compositional averaging of MORB can conceal important variations that are in fact revealing (Niu and Batiza, 1997). For example, average MORB show no Eu anomaly, but actual MORB melts show both positive and negative Eu anomalies (Niu and O'Hara, 2009). In terms of Fe isotopes, it is already clear from Fig. 5 and foregoing discussion that the systematic Fe isotopic variation with MgO in EPR 10°30'N lavas must be caused by fractional crystallization. It follows that the average $\delta^{56}\text{Fe}$ of MORB can neither represent that of primary MORB melt nor their mantle sources. Moreover, it is inappropriate to estimate Fe isotope composition of the bulk Earth using average MORB.

In contrast, the corrected primary MORB melt and the mantle melting models in this study support the idea that the Fe isotope composition of the depleted mantle beneath the EPR is close to chondritic. Combined with estimated $\delta^{56}\text{Fe}$ values for primary melt of global MORB by Sossi et al. (2016), we suggest that the Fe isotope composition of the MORB mantle is most likely close to chondritic. Notably, similar fractional crystallization and parental compositional models have been discussed for OIB by Peters et al. (2019), who suggest that the Piton de la Fournaise parental magma has a Fe isotope composition consistent with extraction from a roughly chondritic mantle. Collectively, it implies that the Fe isotope composition of the accessible Earth is chondritic. Thus, complex models such as evaporation-induced kinetic isotope fractionation during moon-forming giant impact (Poitrasson et al., 2004) or equilibrium Fe isotope fractionation during core formation or Fe disproportionation (Polyakov, 2009; Williams et al., 2012) may not be needed to explain a non-chondritic mantle.

However, we should note that the general understanding is that the carbonaceous chondrite represents the most primitive and most undifferentiated material of the solar system with its composition similar or identical to the solar system (McSween, 1979). The terrestrial planets, including the Earth, thus have the same chondritic composition except for the loss of some volatile elements and late veneer addition of highly siderophile elements (McDonough and Sun, 1995). Yet, by concluding the upper mantle source rocks of basalts as being chondritic or chondrite-like in terms of Fe isotopes, we are assuming bulk Earth is chondritic and the Earth's core that takes up ~90% of the Earth's Fe must also be chondritic. The latter is a rather bold assumption inferred from ~10% of Earth's Fe whose isotope compositions and fractionation remain to be better understood. We thus emphasize that rigorous research is needed to test the implied assumption that the Earth's core has a chondritic Fe isotope composition.

6. CONCLUSION

We report Fe isotope data on MORB melts from the EPR at 10°30'N. Twenty-nine MORB glasses span a wide compositional range in MgO content (1.8–7.4 wt.%) and show a compositional continuum identical to simple liquid lines of descent resulting from varying extent of fractional crystallization. The systematic Fe isotope variation of these samples is best explained by MORB melt evolution dominated by fractional crystallization. That is, early fractionation of olivine, pyroxene and plagioclase gives rise to an Fe enrichment trend and an increase in $\delta^{56}\text{Fe}$. In the later stage of magma evolution when Fe-Ti oxides appear on the liquidus to crystallize, the decrease of FeO^{\dagger} is accompanied by the decrease of $\delta^{56}\text{Fe}$ in the residue melt. This indicates that the $\delta^{56}\text{Fe}$ of average MORB neither represents that of their primary melts nor reflects that of the mantle source. On the other hand, $\delta^{56}\text{Fe}$ of primary melts obtained after correction for the effect of magma different can be well reproduced by partial melting of the mantle. Hence, our study supports the idea that the Fe isotopic composition of the accessible Earth is close to chondritic. This conclusion, however, implies an assumption that the core, which takes up ~90% of the Earth's Fe, must have chondritic Fe isotope composition.

ACKNOWLEDGMENTS

We thank Fang-zhen Teng for providing the MORB data compilation and Paolo A. Sossi for providing the correction tool of iron isotopes to the primary magma composition. Yongsheng He and Jin Li are thanked for providing Fe isotope standards. We thank Bradley J. Peters, Alex McCoy-West and an anonymous reviewer for constructive reviews, and Stefan Weyer for editorial handling. Financial support for this research was provided by the National Natural Science Foundation (NSFC)-Shandong Joint Fund for Marine Science Research Centers (U1606401), China Postdoctoral Science Foundation (2019M652496) and NSFC grants (41630968, 41776067, 41130314) as well as the 111 project (B18048).

APPENDIX A. SUPPLEMENTARY MATERIAL

Supplementary data to this article can be found online at <https://doi.org/10.1016/j.gca.2019.09.031>.

REFERENCES

- Bézos A. and Humler E. (2005) The $\text{Fe}^{3+}/\Sigma\text{Fe}$ ratios of MORB glasses and their implications for mantle melting. *Geochim. Cosmochim. Acta* **69**, 711–725.
- Batiza R., Niu Y., Karsten J., Boger W., Potts E., Norby L. and Butler R. (1996) Steady and non-steady state magma chambers below the East Pacific Rise. *Geophys. Res. Lett.* **23**, 221–224.
- Cao Y., Wang C. Y., Huang F. and Zhang Z. (2019) Iron isotope systematics of the Panzhihua Mafic layered intrusion associated with giant Fe-Ti oxide deposit in the Emeishan Large Igneous Province, SW China. *J. Geophys. Res.: Solid Earth* **124**, 358–375.
- Chen S., Wang X., Niu Y., Sun P., Duan M., Xiao Y., Guo P., Gong H., Wang G. and Xue Q. (2017) Simple and cost-effective methods for precise analysis of trace element abundances in geological materials with ICP-MS. *Sci. Bull.* **62**, 277–289.

- Cottrell E. and Kelley K. A. (2011) The oxidation state of Fe in MORB glasses and the oxygen fugacity of the upper mantle. *Earth Planet. Sci. Lett.* **305**, 270–282.
- Craddock P. R. and Dauphas N. (2011) Iron isotopic compositions of geological reference materials and chondrites. *Geostand. Geoanal. Res.* **35**, 101–123.
- Craddock P. R., Warren J. M. and Dauphas N. (2013) Abyssal peridotites reveal the near-chondritic Fe isotopic composition of the Earth. *Earth Planet. Sci. Lett.* **365**, 63–76.
- Crisp J. A. (1984) Rates of magma emplacement and volcanic output. *J. Volcanol. Geotherm. Res.* **20**, 177–211.
- Danyushevsky L. V. (2001) The effect of small amounts of H₂O on crystallisation of mid-ocean ridge and backarc basin magmas. *J. Volcanol. Geotherm. Res.* **110**, 265–280.
- Danyushevsky L. V. and Plechov P. (2011) Petrolog 3: Integrated software for modeling crystallization processes. *Geochem. Geophys. Geosyst.* **12**.
- Dauphas N., Craddock P. R., Asimow P. D., Bennett V. C., Nutman A. P. and Ohnenstetter D. (2009a) Iron isotopes may reveal the redox conditions of mantle melting from Archean to Present. *Earth Planet. Sci. Lett.* **288**, 255–267.
- Dauphas N., John S. G. and Rouxel O. (2017) Iron isotope systematics. *Rev. Mineral. Geochem.* **82**, 415–510.
- Dauphas N., Pourmand A. and Teng F.-Z. (2009b) Routine isotopic analysis of iron by HR-MC-ICPMS: how precise and how accurate? *Chem. Geol.* **267**, 175–184.
- Dauphas N., Roskosz M., Alp E., Neuville D., Hu M., Sio C., Tissot F., Zhao J., Tissandier L. and Médard E. (2014) Magma redox and structural controls on iron isotope variations in Earth's mantle and crust. *Earth Planet. Sci. Lett.* **398**, 127–140.
- Dauphas N., Teng F.-Z. and Arndt N. T. (2010) Magnesium and iron isotopes in 2.7 Ga Alexo komatiites: mantle signatures, no evidence for Soret diffusion, and identification of diffusive transport in zoned olivine. *Geochim. Cosmochim. Acta* **74**, 3274–3291.
- Elardo S. M., Shahar A., Mock T. D. and Sio C. K. (2019) The effect of core composition on iron isotope fractionation between planetary cores and mantles. *Earth Planet. Sci. Lett.* **513**, 124–134.
- Foden J., Sossi P. A. and Wawryk C. M. (2015) Fe isotopes and the contrasting petrogenesis of A-, I- and S-type granite. *Lithos* **212–215**, 32–44.
- He Y., Ke S., Teng F.-Z., Wang T., Wu H., Lu Y. and Li S. (2015) High-precision iron isotope analysis of geological reference materials by high-resolution MC-ICP-MS. *Geostand. Geoanal. Res.* **39**, 341–356.
- Hibbert K., Williams H., Kerr A. C. and Puchtel I. (2012) Iron isotopes in ancient and modern komatiites: evidence in support of an oxidised mantle from Archean to present. *Earth Planet. Sci. Lett.* **321**, 198–207.
- Hin R. C., Schmidt M. W. and Bourdon B. (2012) Experimental evidence for the absence of iron isotope fractionation between metal and silicate liquids at 1GPa and 1250–1300°C and its cosmochemical consequences. *Geochim. Cosmochim. Acta* **93**, 164–181.
- Huang F., Zhang Z., Lundstrom C. C. and Zhi X. (2011) Iron and magnesium isotopic compositions of peridotite xenoliths from Eastern China. *Geochim. Cosmochim. Acta* **75**, 3318–3334.
- Jochum K. P., Weis U., Schwager B., Stoll B., Wilson S. A., Haug G. H., Andreae M. O. and Enzweiler J. (2016) Reference values following ISO guidelines for frequently requested rock reference materials. *Geostand. Geoanal. Res.* **40**, 333–350.
- Konter J. G., Pietruszka A. J., Hanan B. B., Finlayson V. A., Craddock P. R., Jackson M. G. and Dauphas N. (2016) Unusual $\delta^{56}\text{Fe}$ values in Samoan rejuvenated lavas generated in the mantle. *Earth Planet. Sci. Lett.* **450**, 221–232.
- Liu J., Dauphas N., Roskosz M., Hu M. Y., Yang H., Bi W., Zhao J., Alp E. E., Hu J. Y. and Lin J. F. (2017) Iron isotopic fractionation between silicate mantle and metallic core at high pressure. *Nat. Commun.* **8**, 14377.
- McCoy-West A. J., Fitton J. G., Pons M.-L., Inglis E. C. and Williams H. M. (2018) The Fe and Zn isotope composition of deep mantle source regions: insights from Baffin Island picrites. *Geochim. Cosmochim. Acta* **238**, 542–562.
- McDonough W. F. (2014). Compositional Model for the Earth's Core. pp. 559–577.
- McDonough W. F. and Sun S.-S. (1995) The composition of the Earth. *Chem. Geol.* **120**, 223–253.
- McSween, Jr, H. Y. (1979) Are carbonaceous chondrites primitive or processed? A review. *Rev. Geophys.* **17**(5), 1059–1078.
- Nebel O., Campbell I. H., Sossi P. A. and Van Kranendonk M. J. (2014) Hafnium and iron isotopes in early Archean komatiites record a plume-driven convection cycle in the Hadean Earth. *Earth Planet. Sci. Lett.* **397**, 111–120.
- Nebel O., Sossi P. A., Bénard A., Wille M., Vroon P. Z. and Arculus R. J. (2015) Redox-variability and controls in subduction zones from an iron-isotope perspective. *Earth Planet. Sci. Lett.* **432**, 142–151.
- Niu Y. (2016) The meaning of global ocean ridge basalt major element compositions. *J. Petrol.* **57**, 2081–2103.
- Niu Y. and Batiza R. (1997) Trace element evidence from seamounts for recycled oceanic crust in the Eastern Pacific mantle. *Earth Planet. Sci. Lett.* **148**, 471–483.
- Niu Y., Collerson K., Batiza R., Wendt I. J. and Regelous M. (1999) The origin of E-type MORB at ridges far from mantle plumes: the East Pacific Rise at 11°20'N. *J. Geophys. Res.* **104**, 7067–7087.
- Niu Y. and O'Hara M. J. (2008) Global correlations of ocean ridge basalt chemistry with axial depth: a new perspective. *J. Petrol.* **49**, 633–664.
- Niu Y. and O'Hara M. J. (2009) MORB mantle hosts the missing Eu (Sr, Nb, Ta and Ti) in the continental crust: new perspectives on crustal growth, crust–mantle differentiation and chemical structure of oceanic upper mantle. *Lithos* **112**, 1–17.
- Peters B. J., Shahar A., Carlson R. W., Day J. M. D. and Mock T. D. (2019) A sulfide perspective on iron isotope fractionation during ocean island basalt petrogenesis. *Geochim. Cosmochim. Acta* **245**, 59–78.
- Poitrasson F., Delpech G. and Grégoire M. (2013) On the iron isotope heterogeneity of lithospheric mantle xenoliths: implications for mantle metasomatism, the origin of basalts and the iron isotope composition of the Earth. *Contrib. Mineral. Petrol.* **165**, 1243–1258.
- Poitrasson F., Halliday A. N., Lee D.-C., Levasseur S. and Teutsch N. (2004) Iron isotope differences between Earth, Moon, Mars and Vesta as possible records of contrasted accretion mechanisms. *Earth Planet. Sci. Lett.* **223**, 253–266.
- Poitrasson F., Roskosz M. and Corgne A. (2009) No iron isotope fractionation between molten alloys and silicate melt to 2000 °C and 7.7 GPa: experimental evidence and implications for planetary differentiation and accretion. *Earth Planet. Sci. Lett.* **278**, 376–385.
- Polyakov V. B. (2009) Equilibrium iron isotope fractionation at core-mantle boundary conditions. *Science* **323**, 912–914.
- Regelous M., Niu Y., Wendt J., Batiza R., Grieg A. and Collerson K. (1999) Variations in the geochemistry of magmatism on the East Pacific Rise at 10°30'N since 800 ka. *Earth Planet. Sci. Lett.* **168**, 45–63.
- Roeder P. L. and Emslie R. F. (1970) Olivine-liquid equilibrium. *Contrib. Mineral. Petrol.* **29**, 275–289.
- Schuessler J. A., Schoenberg R. and Sigmarsson O. (2009) Iron and lithium isotope systematics of the Hekla volcano, Iceland—

- evidence for Fe isotope fractionation during magma differentiation. *Chem. Geol.* **258**, 78–91.
- Shahar A., Hillgren V. J., Horan M. F., Mesa-Garcia J., Kaufman L. A. and Mock T. D. (2015) Sulfur-controlled iron isotope fractionation experiments of core formation in planetary bodies. *Geochim. Cosmochim. Acta* **150**, 253–264.
- Siebert J., Badro J., Antonangeli D. and Ryerson F. J. (2013) Terrestrial accretion under oxidizing conditions. *Science* **339**, 1194–1197.
- Sossi P. A., Foden J. D. and Halverson G. P. (2012) Redox-controlled iron isotope fractionation during magmatic differentiation: an example from the Red Hill intrusion, S. Tasmania. *Contrib. Mineral. Petrol.* **164**, 757–772.
- Sun P., Halverson G. P., Nebel O. and Eggins S. M. (2015) Combined separation of Cu, Fe and Zn from rock matrices and improved analytical protocols for stable isotope determination. *Geostand. Geoanal. Res.* **39**, 129–149.
- Sossi P. A., Nebel O. and Foden J. (2016) Iron isotope systematics in planetary reservoirs. *Earth Planet. Sci. Lett.* **452**, 295–308.
- Sun P., Niu Y., Guo P., Chen S., Duan M., Gong H., Wang X. and Xiao Y. (2018) Multiple mantle metasomatism beneath the Leizhou Peninsula, South China: evidence from elemental and Sr-Nd-Pb-Hf isotope geochemistry of the late Cenozoic volcanic rocks. *Int. Geol. Rev.* **61**, 1768–1785.
- Telus M., Dauphas N., Moynier F., Tissot F. L. H., Teng F.-Z., Nabelek P. I., Craddock P. R. and Groat L. A. (2012) Iron, zinc, magnesium and uranium isotopic fractionation during continental crust differentiation: the tale from migmatites, granitoids, and pegmatites. *Geochim. Cosmochim. Acta* **97**, 247–265.
- Teng F.-Z., Dauphas N. and Helz R. T. (2008) Iron isotope fractionation during magmatic differentiation in Kilauea Iki lava lake. *Science* **320**, 1620–1622.
- Teng F.-Z., Dauphas N., Huang S. and Marty B. (2013) Iron isotopic systematics of oceanic basalts. *Geochim. Cosmochim. Acta* **107**, 12–26.
- Weyer S., Anbar A. D., Brey G. P., Münker C., Mezger K. and Woodland A. B. (2005) Iron isotope fractionation during planetary differentiation. *Earth Planet. Sci. Lett.* **240**, 251–264.
- Weyer S. and Ionov D. A. (2007) Partial melting and melt percolation in the mantle: the message from Fe isotopes. *Earth Planet. Sci. Lett.* **259**, 119–133.
- Williams H., Peslier A., McCammon C., Halliday A., Levasseur S., Teutsch N. and Burg J. (2005) Systematic iron isotope variations in mantle rocks and minerals: the effects of partial melting and oxygen fugacity. *Earth Planet. Sci. Lett.* **235**, 435–452.
- Williams H. M. and Bizimis M. (2014) Iron isotope tracing of mantle heterogeneity within the source regions of oceanic basalts. *Earth Planet. Sci. Lett.* **404**, 396–407.
- Williams H. M., McCammon C. A., Peslier A. H., Halliday A. N., Teutsch N., Levasseur S. and Burg J.-P. (2004) Iron isotope fractionation and the oxygen fugacity of the mantle. *Science* **304**, 1656–1659.
- Williams H. M., Wood B. J., Wade J., Frost D. J. and Tuff J. (2012) Isotopic evidence for internal oxidation of the Earth's mantle during accretion. *Earth Planet. Sci. Lett.* **321**, 54–63.
- Zhao X., Zhang H., Zhu X., Tang S. and Tang Y. (2010) Iron isotope variations in spinel peridotite xenoliths from North China Craton: implications for mantle metasomatism. *Contrib. Mineral. Petrol.* **160**, 1–14.
- Zhao X., Zhang H., Zhu X., Tang S. and Yan B. (2012) Iron isotope evidence for multistage melt–peridotite interactions in the lithospheric mantle of eastern China. *Chem. Geol.* **292**, 127–139.
- Zhu C., Lu W., He Y., Ke S., Wu H. and Zhang L. (2018) Iron isotopic analyses of geological reference materials on MC-ICP-MS with instrumental mass bias corrected by three independent methods. *Acta Geochim.* **37**, 691–700.

Associate editor: Stefan Weyer